Stopping and Reversing Sound via Dynamic Dispersion Tuning in a Phononic Metamaterial

Pragalv Karki[1,*] and Jayson Paulose[1,2,†]

[1]*Department of Physics and Institute for Fundamental Science, University of Oregon, Eugene, Oregon 97403, USA*
[2]*Material Science Institute, University of Oregon, Eugene, Oregon 97403, USA*

Slowing down, stopping, and reversing a signal is a core functionality for information processing. Here, we show that this functionality can be realized by tuning the dispersion of a periodic system through a dispersionless, or flat, band. Specifically, we propose a phononic metamaterial based on plate resonators, in which the phonon band dispersion can be modified from an acousticlike to an optical character by modulating a uniform prestress. The switch is enabled by the change in sign of an effective coupling between fundamental modes, which generically leads to a nearly dispersion-free band at the transition point. We demonstrate how adiabatic tuning of the band dispersion can immobilize and reverse the propagation of a sound pulse in simulations of a one-dimensional resonator chain. Our study relies on the basic principles of thin-plate elasticity independently of any specific material, making our results applicable across varied length scales and experimental platforms. More broadly, our approach could be replicated for signal manipulation in photonic metamaterials and electronic heterostructures.

I. INTRODUCTION

The tunability of sound transport properties after fabrication is a prominent feature underlying the appeal of phononic metamaterials [1]. In periodic structures, tunability can be achieved by modifying the band structure of vibrational excitations, which determines both the frequency ranges of sound insulation (via bandgaps) and the group velocity of sound propagation (via the frequency-momentum relationship or dispersion relation). Metamaterials with tunable phononic bands have been proposed that use modulation methods as varied as buckling [2,3], large structural deformations [4–6], electrical [7–9] and optical [10] actuation, and prestress modulation [11–15]. While most of these proposals have targeted the tuning of bandgaps, several works [6–8,14] have highlighted the ability to change group velocities by tuning the dispersion relation as a promising direction for adapting a metamaterial to different static conditions. However, the dynamic control of dispersion remains unexploited as a mechanism for signal manipulation.

In this work, we demonstrate how to stop and reverse signals in a tunable metamaterial by dynamically changing the dispersion character of an entire band during signal propagation. Specifically, we describe a physical

mechanism to flip the sign of the group velocity across all quasimomenta (i.e., wavevectors associated with the excitations of the periodic lattice), thereby reversing the propagation direction of wave pulses (Fig. 1). A unique aspect of our approach is that the group velocity vanishes throughout the band at the point of sign switching, giving rise to a flat phononic band that can trap a signal for subsequent release when required. Using full-wave finite-element simulations, we show how adiabatic tuning of the dispersion allows us to store and reverse a sound pulse in a waveguide—a functionality that has potential applications in acoustic sensing [16,17], signal processing [18], and computation [19–21].

We accomplish the desired change in dispersion by manipulating the coupling between adjacent degrees of freedom in a periodic structure. In our design, the relevant degrees of freedom are the fundamental (i.e., lowest-frequency) transverse vibrational modes of free-standing thin-plate mechanical resonators supported by a rigid frame. However, the underlying physical principle is independent of the specific type of excitation, as illustrated in Fig. 1 for the lowest excitation band of coupled modes on an infinite periodic chain. In a tight-binding description of coupled excitations, the Bloch state at the band center (quasimomentum $q_x = 0$) is constructed from eigenmodes in a "bonding" configuration (adjacent eigenmodes are in phase), while the state at the band edge ($q_x = \pm\pi/a$, where a is the lattice constant) is an assembly of out-of-phase or "antibonding" pairs. If the bonding state for a pair of
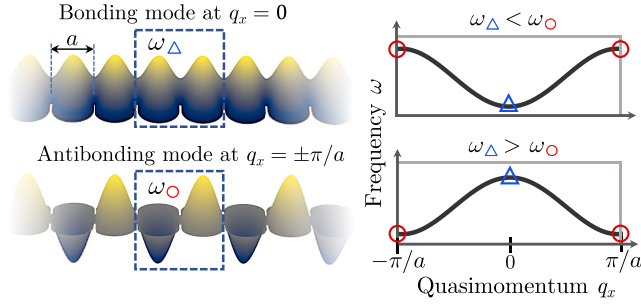
———————
*pragalvk@uoregon.edu
†jpaulose@uoregon.edu

FIG. 1. Relationship between paired-mode frequencies and dispersion, illustrated for a periodic system with lattice constant a. Left: the Bloch mode of the lowest band at $q_x = 0$ is composed of a chain of in-phase or bonding pairs of fundamental excitations (top), whereas the mode at $q_x = \pm \pi/a$ is composed of out-of-phase or antibonding pairs (bottom). Right: schematic of the different band dispersion relations when the frequency of the bonding pair $\omega_\triangle$ is lower (top) or higher (bottom) than the antibonding pair frequency $\omega_\circ$.

building blocks is at a lower frequency than the antibonding one, the dispersion relation must increase from the band center to the band edge. In contrast, if the antibonding configuration has a lower frequency, the dispersion relation is a decreasing function of the quasimomentum magnitude. Therefore, flipping the bonding character of pairwise couplings across a periodic structure can reverse the group velocity (the slope of the dispersion relation) throughout the band. Below, we show that the mechanics of thin plates under tension enables precisely such a reversal (Fig. 2). However, the approach could be replicated in other wave systems where the bonding character of paired degrees of freedom can be controlled, such as photonic crystals [22] or electronic heterostructures [23,24].

II. THEORETICAL FRAMEWORK

A. Model of coupled plate resonators

We model the out-of-plane vibrations of suspended resonators with a defined edge geometry using the partial differential equation for the transverse displacement field $u(x, y)$ of an elastic plate with mass per unit area ρ, bending modulus D, subjected to a uniform in-plane tension T', and clamped to a rigid plane curve along its edges [25]:

$$\rho \frac{\partial^2 u}{\partial t^2} + D \nabla^4 u - T' \nabla^2 u = 0 \quad \text{on domain,}$$
$$u = \nabla u = 0 \quad \text{on boundary.} \tag{1}$$

While the bending modulus and density are material properties, the tension is an externally imposed stress that can be tuned through external manipulation (e.g., via laser heating [26] or electrostatic gating [8]).

To perform our analysis without making explicit choices for the physical dimensions and material parameters,
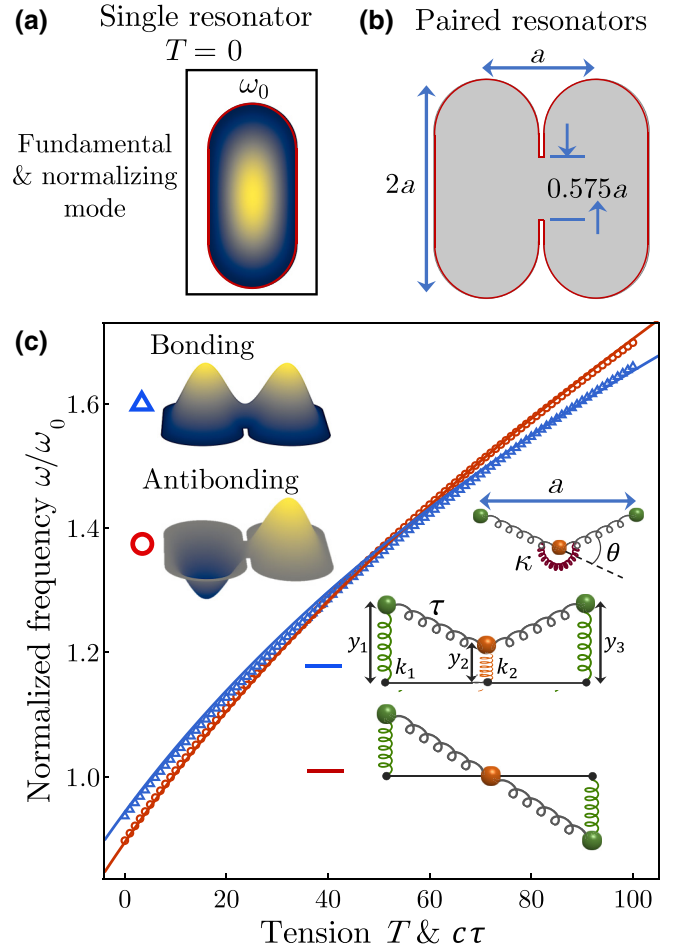

FIG. 2. (a) Geometry of a single resonator supported by a rigid boundary (red edge) and free to vibrate in the interior. Color intensity represents the displacement field of the fundamental mode at zero tension, whose frequency ω_0 is used as the normalizing frequency throughout the study. (b) Geometry of a resonator pair including the junction. This specific junction geometry is chosen to maximize mode separation at $T = 0$, but the effect persists for other narrow junctions. (c) Frequency of the two lowest eigenmodes of the resonator pair as a function of rescaled tension. Symbols are from finite-element simulations, and distinguish the bonding character of the corresponding eigenmode. Left inset shows numerically determined eigenmodes at $T = 0$. Solid lines show the two lowest eigenfrequencies of the discrete dynamical matrix, Eq. (4). Dimensionless parameters T (continuum model) and τ (discrete model) are related via $T = c\tau$, where $c = 47.5$ is a geometry-dependent linear mapping constant. Right inset shows tensile and torsional springs in the discrete model, and examples of bonding (blue) and antibonding (red) modes.

we nondimensionalize the continuum plate equations, Eqs. (1), by performing a change of variables [27] using the lattice constant a and the time scale $\sqrt{\rho a^4 / D}$ as the length and time units. Upon defining $\bar{x} = x/a$, $\bar{y} = y/a$,

$\bar{t} = t\sqrt{D/(\rho a^4)}$, Eqs. (1) yield

$$\frac{\partial^2 u}{\partial \bar{t}^2} + \bar{\nabla}^4 u - T\bar{\nabla}^2 u = 0 \quad \text{on domain},$$

$$u = \bar{\nabla} u = 0 \quad \text{on boundary}. \tag{2}$$

Once the boundary geometry is specified, Eqs. (2) show that the nondimensionalized dynamics depend on a single dimensionless parameter—the rescaled tension $T \equiv T'a^2/D$, which serves as the tunable physical quantity in our study. In the remainder of this manuscript, we drop the bar for clarity; the variables x, y, t, and the gradient operator ∇ are understood to refer to the rescaled coordinates.

For a particular resonator geometry, oscillatory solutions to Eqs. (2) can be expanded in terms of normal modes $u_i(x,y)e^{-i\omega_i t}$ indexed by the variable i, where the functions $u_i(x,y)$ and oscillation frequencies ω_i solve the eigenvalue problem

$$\nabla^4 u_i - T\nabla^2 u_i = \omega_i^2 u_i \tag{3}$$

together with the boundary conditions. Normal mode displacements and frequencies are computed using finite-element analysis; see Appendix A for details. We use the lowest-frequency, or fundamental, mode of a single resonator with frequency ω_0 [Fig. 2(a)] as the basic degree of freedom in our system and consider the collective modes that arise upon coupling fundamental modes across multiple resonators through junctions as shown in Fig. 2(b).

For narrow junctions, the two lowest eigenmodes of a pair of resonators can be identified with a bonding and an antibonding configuration of the fundamental modes of the individual resonators [Fig. 2(c)]. In the absence of a bending stiffness, Eq. (3) reduces to a Laplacian eigenfunction problem, for which the maximum principle dictates that the eigenfunction with the lowest eigenvalue must be of fixed sign over the domain. As a result, the bonding mode is guaranteed to be lower in frequency than the antibonding mode in the $D \to 0$, or $T \to \infty$, limit. However, the maximum principle does not hold for the *biharmonic* eigenfunction problem obtained in the $T \to 0$ limit of Eq. (3), for which domains with nonconvex boundaries have been found to favor lowest-frequency eigenfunctions with sign changes within the domain [28,29]. Therefore, we expect the antibonding mode to be at a lower frequency when the external tension is set to zero, but to switch to a higher frequency relative to the bonding mode at large tensions. Numerical solutions of the two lowest eigenmodes of the resonator pair, obtained via finite-element analysis (Appendix A), confirm this expectation [Fig. 2(c)]. The lowest-frequency mode switches from antibonding to bonding type at a geometry-dependent threshold tension

$T^* \approx 45$, at which the two lowest normal mode frequencies coincide to signify a degeneracy of the antibonding and bonding modes.

Since the crossing behavior fundamentally arises from the competition between bending and tension in thin-plate mechanics, it is not restricted to our particular choice of single-resonator geometry in Fig. 2. While details such as the magnitude of the threshold tension are geometry dependent, the basic mechanism is generic to a wide range of resonator geometries when connected by a narrow junction. Furthermore, while we have used the clamped boundary condition to capture the typical edge constraint for micromechanical resonators mounted on semiconductor substrates [30], the switch in bonding character also occurs for simply supported edges (Dirichlet boundary conditions), as we verify in Appendix B.

B. Minimal model of mode-crossing mechanism

The balance between bending and tension that drives the eigenmode crossing can be captured in a simpler discrete model of coupled harmonic oscillators. The fundamental mode of an isolated resonator is modeled as a harmonic degree of freedom y confined to the vertical direction, with a unit mass and spring constant $\tilde{k}_1$. Building on past approaches [31], we then attempt to build the normal modes of coupled resonators by incorporating couplings among fundamental modes on adjacent oscillators, using, e.g., a horizontal spring under tension. However, according to the von Neumann–Wigner theorem, coupling two degrees of freedom would generically create an *avoided* crossing of eigenvalues of the coupled system upon varying the coupling strength, in contrast to the observed behavior in Fig. 2(c).

The key to obtaining the correct crossing behavior is to incorporate the plate deformation at the junction into the reduced description as an additional degree of freedom—specifically, a unit mass on a vertical spring with stiffness $\tilde{k}_2 > \tilde{k}_1$. This mass is coupled to the resonator degrees of freedom through tensed and torsional springs, as shown schematically in the right insets of Fig. 2(c). The coupling of the resonator modes due to tension is encoded in harmonic springs connecting each mode mass to the junction mass, which are prestressed with a tensile force $\tilde{\tau}$. These contribute a potential energy $U_s = \tilde{\tau}[(y_1 - y_2)^2 + (y_2 - y_3)^2]/a$ to vertical displacements. The bending stiffness penalizes geometric curvature at the junction; we include this effect by defining a torsional spring that favors collinearity of the two tensile springs with associated harmonic energy $U_b = \tilde{\kappa}(1 - \cos\theta) \approx 2\tilde{\kappa}(y_1 - 2y_2 + y_3)^2/a^2$. By choosing ω_0^{-1} and a as the time and length units, respectively, we obtain a discrete model with four dimensionless parameters k_1, k_2, τ, and κ (the absence of the tilde indicates nondimensionalized quantities); see Appendix C.

The nondimensionalized stiffness matrix describing the dynamics of the three harmonic degrees of freedom is

$$\mathbf{K} = \begin{pmatrix} k_1 + \tau + \kappa & -\tau - 2\kappa & \kappa \\ -\tau - 2\kappa & k_2 + 2\tau + 4\kappa & -\tau - 2\kappa \\ \kappa & -\tau - 2\kappa & k_1 + \tau + \kappa \end{pmatrix}. \quad (4)$$

The two lowest eigenfrequencies of the stiffness matrix correspond to the coupled modes that arise from weak coupling of the fundamental modes (Appendix D); the third mode is considerably higher in frequency and is not relevant to our analysis. When $\tau = 0$, the antibonding configuration has a lower frequency because the torsional spring remains undistorted [Fig. 2(c), lower right inset]. Upon increasing τ with other parameters kept fixed, the bonding configuration becomes increasingly favored because it costs lower tensile energy, and the two modes become degenerate at $\tau = \sqrt{(3\kappa/2)^2 + \kappa(k_2 - k_1)} - 3\kappa/2$. If a linear relationship is assumed between the dimensionless tensions τ and T, the minimal model with four fit parameters quantitatively captures the evolution of the normal mode frequencies from the continuum model [compare the symbols and solid lines in Fig. 2(c)]. Details of the fitting procedure are provided in Appendix E.

III. RESULTS

A. Dispersion relation and flat band

To illustrate the consequences of the switch in parity of the lowest-frequency pair eigenmode on sound transport, we compute the mode spectrum for an infinite one-dimensional (1D) chain of coupled resonators as a function of the quasimomentum q_x that indexes the Bloch eigenfunctions $u_{q_x}(x,y) = e^{iq_xx}\phi_{q_x}(x,y)$. For the continuum system, whose unit cell is depicted in Fig. 3(a), the numerically determined spectrum (Appendix A) consists of infinitely many bands within the Brillouin zone $-\pi/a < q_x < \pi/a$, but the lowest band is built primarily from the fundamental modes of the individual resonators. The dispersion relation $\omega(q_x)$ for this band is captured in the reduced description with a two-mass unit cell shown in Fig. 3(b). The Fourier-transformed stiffness matrix obtained by upgrading Eq. (4) to a periodic chain is

$$\mathbf{K}(q_x) = \begin{pmatrix} a + b\cos q_x & -c(1 + e^{-iq_x}) \\ -c(1 + e^{iq_x}) & d \end{pmatrix}, \quad (5)$$

where $a = k_1 + 2\tau + 2\kappa$, $b = 2\kappa$, $c = \tau + 2\kappa$, and $d = k_2 + 2\tau + 4\kappa$. The frequency bands are then solved via $|\mathbf{K}(q_x) - \omega(q_x)^2\mathbf{I}| = 0$.

Dispersion relations for the lowest band, computed using both the continuum and the discrete descriptions, are shown in Fig. 3(c) for three values of the globally applied plate tension. Changing free parameters τ and k_1 in the discrete model effectively captures the changing of
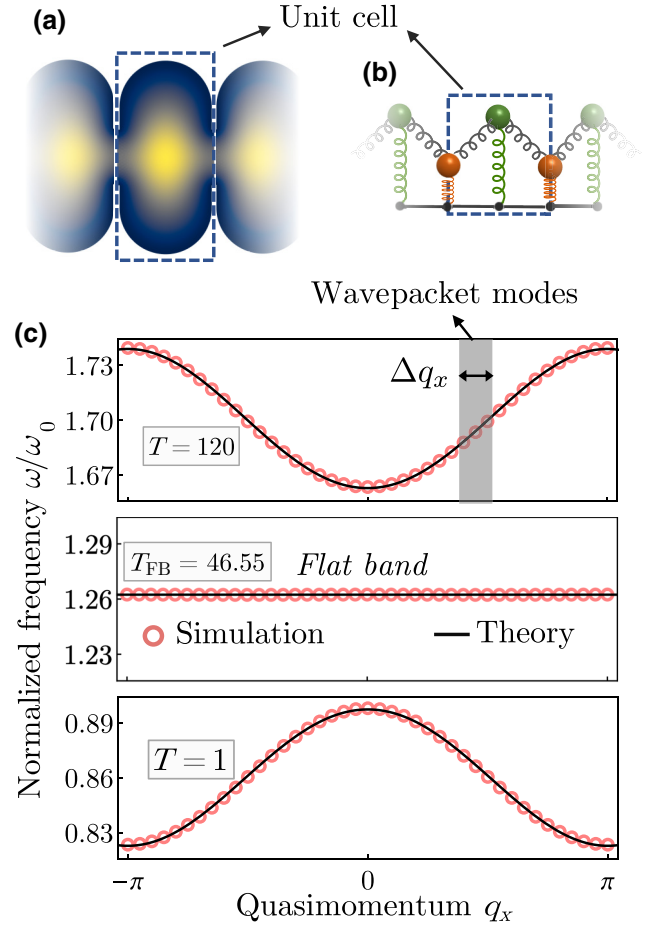

FIG. 3. Dispersion relation of the fundamental band. (a) Unit cell of the continuum model, with intensity variation representing the displacement of the Bloch eigenmode at $q_x = 0$ from finite-element calculations. (b) Unit cell of the discrete model. (c) Band structures of the continuum model at three values of rescaled tension (symbols), compared to bands computed from the discrete model (solid lines). Fit parameters τ and k_1 for different tensions: $T = 1 \rightarrow \{\tau, k_1\} \approx \{0.3195, 0.0381\}$, $T = 46.55 \equiv T_{\text{FB}} \rightarrow \{\tau, k_1\} \approx \{0.5217, 0.5502\}$, and $T = 120 \rightarrow \{\tau, k_1\} \approx \{0.7677, 1.4888\}$; see Appendix E for details of fitting procedure. Shaded region shows the quasimomentum range used to create the Gaussian wavepacket for the dynamical simulation.

T in the continuum model (Appendix D). We find that the band changes from optical type (frequency decreasing with quasimomentum) to acoustic type (frequency increasing with quasimomentum) as the tension is increased, in line with our expectation (Fig. 1). At a special value of the rescaled tension, the band becomes nearly dispersion-free, or flat. In the discrete model, we analytically establish the existence of a band with $\partial\omega/\partial q_x = 0$ throughout the Brillouin zone when the condition

$$\tau = \sqrt{(2\kappa)^2 + \kappa(k_2 - k_1)} - 2\kappa \quad (6)$$

is satisfied (see Appendix F for details), so a tension value leading to a perfectly flat band can always be found provided $k_2 > k_1$. In the continuum model, the dispersion does not completely vanish; however, the bandwidth is limited to $10^{-3}\%$ of the mean band frequency. This minute deviation from a perfectly flat band can be reproduced in the discrete model by adding one more torsional spring to the unit cell, centered on the resonator mass (Appendix G).

We note here that the lowest frequency in the periodic system does not go to zero at $q_x = 0$ or $q_x = \pi$, i.e., a low-frequency bandgap exists in the resonator system. This bandgap is a consequence of the finite frequency of the fundamental mode. When the tension is set to zero, the vibrational frequency of a continuum displacement field scales as $\sqrt{D/(\rho l^4)}$, where l is the shortest length scale of variations of the displacement field. For a single resonator, l is at most some fraction of a and the fundamental frequency is of order $\sqrt{D/(\rho a^4)}$ with a prefactor larger than one [numerically, we find that $\omega_0 \approx 27.3\sqrt{D/(\rho a^4)}$ in physical units, consistent with the apparent variation of the displacement field that happens over roughly a third of the resonator width in Fig. 2(a)]. For an infinite 1D chain

of resonators, the lowest frequency remains of order ω_0 because the narrow junctions only weakly perturb the adjacent modes and the displacement fields are still restricted by the resonator width a. If we were to widen the junctions, the lowest frequency of the band would drop, but it would still be bounded from below by the resonator height, $l \lesssim 2a \Rightarrow \omega \gtrsim 4\sqrt{D/(\rho a^2)}$ and a finite bandgap is always expected. By contrast, for a two-dimensional resonator array, we could nearly eliminate the bandgap by widening the coupling junctions in both directions. In that case, the vibrational response of the lowest-frequency Bloch mode would approach that of a square plate of infinite dimension, which truly goes to zero as $l \to \infty$.

B. Slowing, stopping, and reversing a sound pulse

As a prototypical example of manipulating a signal by dynamically tuning the dispersion through a flat band, we consider the evolution of a Gaussian wavepacket under uniform adiabatic modulation of the global tension in a resonator array. We perform full-wave simulations of the continuum model via a finite-element method, and classical dynamics simulations of the discrete mass-spring
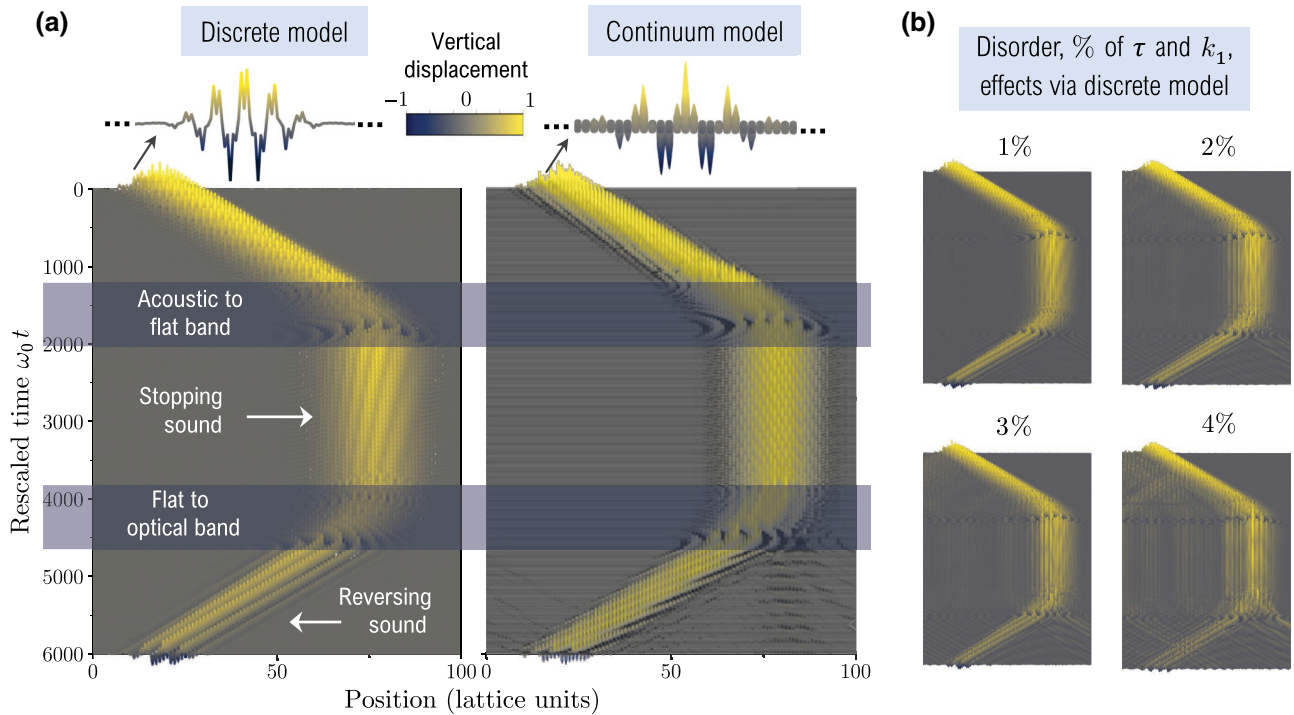

FIG. 4. (a) Sound pulse reversal through dynamic dispersal tuning. Color map shows the vertical displacement evolution of Gaussian wavepackets in dynamical simulations of a linear chain of coupled resonators, for both the discrete (left) and the continuum (right) models. Initial pulses are shown for both systems at the top. Time advances from top to bottom; horizontal axis is position along the chain. Shaded time intervals are periods during which the dispersion is varied along a linear ramp connecting initial to final parameter values as described in the text. (b) Disorder effects on wave packet manipulation with a quenched disorder of 1%–4% of τ and k_1 throughout the chain. Dynamically slowing and stopping the pulse is robust up to 3% disorder and the reversal is robust up to 2%. At higher disorder levels, reversal is partially successful for this set of parameters, but a considerable amount of energy is lost to spurious modes.

model via the velocity Verlet algorithm (Appendix H). For both models, a 1D array of 100 unit cells is initialized with a wavepacket built from the band corresponding to $T = 120$ in Fig. 4. The Bloch eigenfunctions $\boldsymbol{\phi}_{q_x}$ are used to construct a sound pulse using the equation

$$\mathbf{u}(n,t) = \sum_{q_x} \boldsymbol{\phi}_{q_x} e^{i[q_x n - \omega(q_x)t]} e^{-[(q_x - q_0)/\Delta q_x]^2}, \quad (7)$$

where $\mathbf{u}(n,t)$ is the vector of displacements of the nth unit cell at time t, and the sum is over all allowed discrete quasimomenta q_x. In the discrete model, $\boldsymbol{\phi}_{q_x}$ and $\mathbf{u}$ are 2 vectors, while in the continuum model their length is determined by the mesh size of the finite-element discretization. The pulse is initialized at $t = 0$ with plane-wave weights centered at $q_0 = 1.2$ with normal deviation $\Delta q_x = 0.25$ [shaded region in Fig. 3(c)]. The resulting pulse profile is localized to roughly 50 unit cells.

The subsequent evolution of the sound pulse is shown in Fig. 4, which tracks the instantaneous position along the chain as a function of time. Video 1 demonstrates the phenomenon in a full-wave finite-element simulation of the continuum model. During the evolution, the dispersion is dynamically tuned at two separate intervals (shaded regions in Fig. 4) by varying T in the continuum model and the parameters $\{\tau, k_1\}$ in the discrete model. Outside

these intervals, the effective tension T is maintained at the constant values depicted in Fig. 3(c). At $T = 120$, the wavepacket has a positive group velocity (positive slope of the dispersion relation at q_0), and travels to the right (Fig. 4, top). The tension is then reduced over roughly 600 oscillation cycles towards the value $T = T_{FB}$ with zero group velocity (upper shaded region in Fig. 4). The slow modulation arrests the pulse, which oscillates in place with minimal distortion when the tension is maintained at T_{FB} (Fig. 4, middle). Finally, the tension is reduced further to $T = 1$ at which the wavepacket group velocity is negative [Fig. 3(c), bottom panel]; this change reverses the propagation direction of the pulse (Fig. 4, bottom).

To approximate unavoidable losses in real systems, the simulations reported in Fig. 4 included linear drag forces that recreate a quality factor (Q factor) of $Q \approx 6500$ (Appendix H). While the energy density of the pulse decays as a result, the damping does not significantly distort the pulse profile or interfere with the expected zero group velocity (in contrast to metamaterials that attempt to generate a vanishing group velocity via local resonances [32]). Quality factors of order 10^4 are well within achievable limits for plate resonators, as discussed below. The dynamic tuning could also be executed over fewer oscillations in a system with lower Q, at the cost of increased energy leakage into spurious modes.
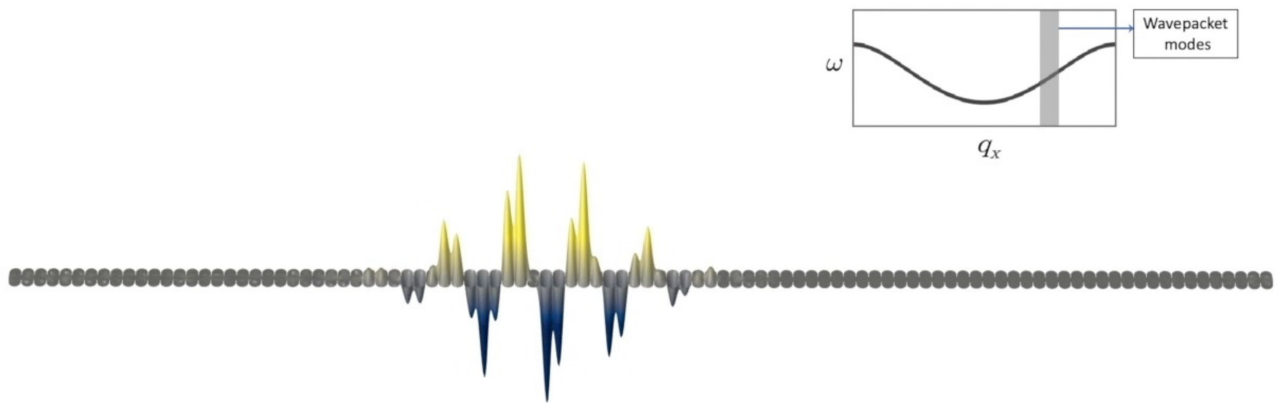
VIDEO 1. Full-wave finite-element simulation that shows the stopping and reversing of a sound pulse through dynamic dispersion tuning. The image above shows a single frame from the video. The video starts with a wavepacket prepared at the left end of the 1D array with a positive group velocity moving to the right. The wavepacket is stopped and reversed by adiabatically tuning the tension, as described in the text. The corresponding change in the dispersion is displayed in the inset on the upper right. The wavevector components comprising the wavepacket are highlighted in gray.

IV. DISCUSSION AND CONCLUSION

A. Considerations for practical realization

1. Tunability and losses

Experimental implementations of our proposal would require plate resonator arrays with high quality factors and tunable in-plane tension. Micromechanical systems based on two-dimensional materials are a prime candidate [8,33]. The membranes are suspended over voids fabricated in semiconductor substrates with the desired metamaterial geometry, and the boundaries are restricted by adhesion of the membrane to the semiconductor at the void boundaries. Prestress modulation of phonon bands via electrostatic backgating has been demonstrated in SiN resonator arrays with $Q \approx 1,700$ [8], and Q factors as high as 10^8 have been reported for individual SiN resonators [34]. Graphene-based resonator arrays [33] can be tuned via electrostatic [35] or thermally induced [26] prestresses; Q factors of order 10^5 have been reported [36,37].

2. Disorder

Another important factor to consider for practical realizations is the effect of disorder due to nonuniformities in fabrication. Finite mesh effects introduce a small amount of spatial disorder in the continuum simulations, which induces energy leakage from the manipulated wavepacket into spurious modes, as can be observed in the lower-right corner of Fig. 4(a). This effect can be reproduced and further investigated in the discrete model by deliberately introducing known amounts of quenched disorder in the effective stiffness parameters. Specifically, we randomly perturb the parameters τ and k_1 to lie within a specified percentage of the parameter values at $T = 1$. The stiffness perturbation on each spring is a random variable that is kept constant for the duration of the simulation to recreate the effect of quenched disorder in the fundamental mode frequencies of the resonators. We find that the pulse reversal is robust up to 3% disorder; see Fig. 4(b). This amount of precision is well within achievable levels for micromechanical systems; for instance, Cha and Daraio [8] estimated parameter variations of far less than 1% across a nanoelectromechanical resonator array. Furthermore, the fundamental mode frequencies of membrane-based resonators can be individually corrected after fabrication using photodoping and electrostatic backgating to achieve the required spatial uniformity [38].

B. Future directions

Besides enabling signal reversal through dynamic dispersion tuning, the physical mechanism reported here also provides a means to realizing flat bands. Like their counterparts in electronics [39] and photonics [40], phononic flat bands [31,41–43] are expected to have interesting transport, localization, and topological properties. Our design,

which is a phononic analog of recipes for designing isolated electronic [44] and photonic [45] flat bands, can be extended to two-dimensional arrays and combined with lattice-based strategies to generate additional classes of flat bands [44,46]. Although we focus on slow parameter modulation in this work, faster dynamic modulation of pre-stresses could enable non-Hermitian and active topological phenomena [47–51]. Discoveries of such phenomena could be aided by the analytically tractable discrete model that quantitatively reproduces the numerically solved continuum dynamics (Fig. 4). Beyond elasticity, modifying the bonding character of paired degrees of freedom has also been demonstrated in photonics [22], quantum dots [23], and superconductors [52], and has been proposed as a band-tuning mechanism for ultracold atoms [24]. Our basic approach, summarized in Fig. 1, could be explored in these systems as a route to tunable dispersion and controlled manipulation of photonic and electronic wavepackets.

APPENDIX A: FINITE-ELEMENT ANALYSIS OF THE CONTINUUM MODEL

Finite-element analyses are carried out using the commercially available package COMSOL Multiphysics®. The *general form pde* module is used to define an eigenvalue problem based on a fourth-order partial differential equation describing thin-plate elasticity,

$$\nabla \cdot [(u_{xxx} + 2u_{xyy} - Tu_x)\hat{x} + (u_{yyy} - Tu_y)\hat{y}] = \lambda u, \quad \text{(A1)}$$

where subscripts denote partial derivatives of u with respect to those coordinates. The Dirichlet boundary condition $u = 0$ and Neumann boundary conditions $u_x = u_y = 0$ satisfy the clamped boundary condition. Simplifying Eq. (A1) gives $\nabla^4 u - T\nabla^2 u = \lambda u$, which is the desired eigenvalue problem. The simulation methods are tested by comparing numerically derived eigensolutions for the square Laplacian plate (setting $D \to 0$) and circular clamped biharmonic plate (setting $T \to 0$) to known analytical results.

The continuum thin-plate resonator model has infinitely many bands, of which a subset are obtained numerically. In Fig. 5, the first eight bands and the eigenfunctions associated with those bands are shown as an example. In this study, we focus solely on the lowest band, which is
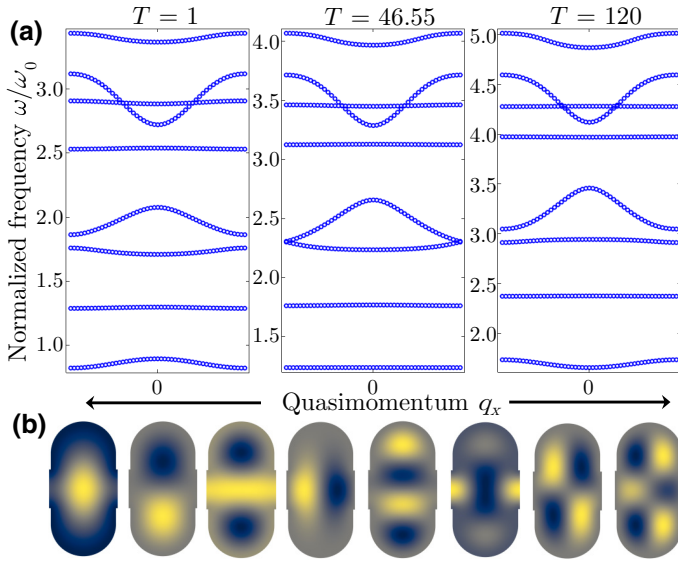
FIG. 5. Eight frequency bands (a) and their eigenfunctions (b) for three different tension T values. The change in the dispersive character of the first band intermediated by a flat band can be seen with increasing tension. Displacements in the second and fifth modes (b) can be seen to be isolated from neighboring resonators, resulting in mostly nondispersive bands (a) throughout different tension values. The third and fourth modes have a band touching at the corners of the Brillouin zone at the flat band tension $T = 46.55$, suggesting possible band inversion. The sixth and seventh modes have a band crossing and the eighth mode simply changes its band width with increasing tension.

built primarily from the lowest-frequency, or fundamental, modes of individual resonators. This is apparent from the mode shape of the Bloch eigenfunction in Fig. 5(b), which mirrors the mode shape of the single-resonator fundamental mode.

APPENDIX B: INSENSITIVITY TO BOUNDARY CONDITIONS

The bonding and antibonding mode flipping mechanism is insensitive to whether the domain boundary is clamped or simply supported (Dirichlet boundary condition only). In Fig. 6, the flipping mechanism is shown for the simply supported case for two different tension values, $T = 1$ and $T = 120$.

Having a junction between the resonators is more important than details of the boundary condition for the eigenmode switching. A clamped boundary condition is used in this study since that is the norm in experimental studies of membrane resonators.

APPENDIX C: NONDIMENSIONALIZATION OF THE DISCRETE MODEL

The Newtonian mechanics of the spring-mass chain, with all points assigned a mass m, is described by the

FIG. 6. Eigenmodes and normalized frequencies of paired resonators with simply supported boundaries. At $T = 1$, the system is in the bending dominated region and hence the antibonding mode has a lower energy and at $T = 120$ the system is in the tension dominated region where the bonding mode has a lower energy.

second-order differential equation

$$m\frac{d^2\mathbf{y}}{d\tilde{t}^2} + \beta\frac{d\mathbf{y}}{d\tilde{t}} + \tilde{\mathbf{K}}\mathbf{y} = 0, \tag{C1}$$

where $\mathbf{y} = \{y_1, y_2, \ldots\}$ is the vector of vertical displacements and $\tilde{\mathbf{K}}$ is the stiffness matrix incorporating the effect of the on-site, tensed, and torsional springs. For the three-site model in Fig. 2 of the main text, the stiffness matrix reads

$$\tilde{\mathbf{K}} = \begin{pmatrix} \tilde{k}_1 + \frac{\tilde{\tau}}{\ell} + \frac{\tilde{\kappa}}{\ell^2} & -\frac{\tilde{\tau}}{\ell} - \frac{2\tilde{\kappa}}{\ell^2} & \frac{\tilde{\kappa}}{\ell^2} \\ -\frac{\tilde{\tau}}{\ell} - \frac{2\tilde{\kappa}}{\ell^2} & \tilde{k}_2 + \frac{2\tilde{\tau}}{\ell} + \frac{4\tilde{\kappa}}{\ell^2} & -\frac{\tilde{\tau}}{\ell} - \frac{2\tilde{\kappa}}{\ell^2} \\ \frac{\tilde{\kappa}}{\ell^2} & -\frac{\tilde{\tau}}{\ell} - \frac{2\tilde{\kappa}}{\ell^2} & \tilde{k}_1 + \frac{\tilde{\tau}}{\ell} + \frac{\tilde{\kappa}}{\ell^2} \end{pmatrix}, \tag{C2}$$

where ℓ is the horizontal spacing between the masses. To build a discrete model with dimensionless parameters that can be related to the continuum system, we choose ω_0^{-1} and a as time and length units, respectively. The distance between primary on-site degrees of freedom y_i and y_{i+2} is also set to be a, so that $\ell = a/2$. Upon defining the rescaled time $t = \omega_0\tilde{t}$, spring stiffnesses $k_i = \tilde{k}_i/m\omega_0^2$, the tension $\tau = 2\tilde{\tau}/am\omega_0^2$, and the torsional stiffness $\kappa = 4\tilde{\kappa}/a^2m\omega_0^2$, we obtain the equation

$$\frac{d^2\mathbf{y}}{dt^2} + 2\zeta\frac{d\mathbf{y}}{dt} + \mathbf{K}\mathbf{y} = 0, \tag{C3}$$

where $\mathbf{K}$ is the nondimensionalized stiffness matrix reported in the main text, and $\zeta = \beta/(m\omega_0)$ is the damping ratio. The quality factor is given by $Q = 1/2\zeta$. All the parameters presented in the main text for the discrete model without the tilde symbol are nondimensionalized versions.

APPENDIX D: THREE-SITE REDUCED MODEL AND THE INFINITE CHAIN

The eigenfrequencies of the three-site reduced model are solved via $|\mathbf{K} - \omega^2 \mathbf{I}| = 0$ with

$$\omega_1^2 = k_1 + \tau,$$
$$\omega_{2,3}^2 = 3\alpha + k_1 + k_2 \pm \sqrt{9\alpha^2 + (k_2 - k_1)(2\alpha + k_2 - k_1)},$$

$$\text{(D1)}$$

where $\alpha = \tau + 2\kappa$. The corresponding eigenvectors are visualized in Fig. 7. The first two modes can be interpreted as antibonding and bonding modes of the continuum system, respectively. The third mode is considerably separated from the first two modes in frequency for the fit parameters obtained in the main text, and is not considered in this study.

1. Infinite chain

The stiffness matrix for an infinite 1D chain of the discrete system takes the form

$$\mathbf{K}_\infty = \begin{pmatrix} \vdots & & \ddots & & & & \vdots \\ \cdots & \kappa & -\tau - 2\kappa & V_1 & -\tau - 2\kappa & \kappa & \cdots \\ \cdots & 0 & 0 & -\tau - 2\kappa & V_2 & -\tau - 2\kappa & \cdots \\ \vdots & & & & \ddots & & \vdots \end{pmatrix}, \qquad \text{(D2)}$$

where $V_1 = k_1 + 2\tau + 2\kappa$ and $V_2 = k_2 + 2\tau + 4\kappa$ are on-site spring stiffnesses. The next-nearest coupling between the sites with spring stiffness k_1 arise due to the torsional spring at the junction. The fourier-transformed version of this infinite matrix is shown in Eq. (3) of the main text.

APPENDIX E: FITTING PROCEDURE FOR REDUCED MODEL PARAMETERS

Given our choice of physical units, the dimensionless parameters for the discrete model are fixed by fitting the eigenfrequencies of the discrete model to the dimensionless frequencies ω/ω_0 from the continuum finite-element analysis.

1. Three-site discrete model

For the analysis of the resonator pair (Fig. 2), we aim to recover the change in frequency of the two lowest modes
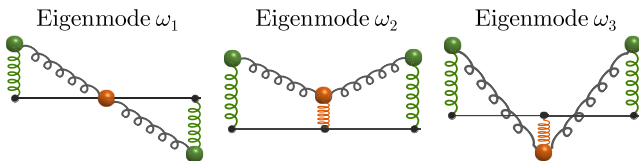

FIG. 7.　Eigenmodes of the three-site reduced model. In addition to the springs shown in this figure, torsional springs are also attached to the middle masses, as shown in the bottom-right inset of Fig. 2(c) in the main text.

upon varying the prestress T in the continuum model by varying the tension τ in the reduced model, keeping all other dimensionless parameters fixed. While T and τ are related, they are different physical quantities (T is a force per unit length for the elastic plate, whereas τ is a tensile force on the horizontal springs). We assume a simple linear relation $T = c\tau$, where c is a constant parameter, and find that this relation is sufficient to recover the mode-crossing behavior.

Given the exact frequencies of the discrete model, Eq. (D1), the parameter value $k_1 = 0.8000$ is fixed by equating it to the square of the antibonding mode frequency from the continuum model at $T = \tau = 0$. The complete relationship between frequency and prestress (tension) for this mode is then quantitatively recovered by setting $c = 47.5$. Having set these two parameters, the remaining parameters $k_2 = 35$ and $\kappa = 0.0450$ are fixed by fitting the analytical form for ω_2 from Eq. (D1) to the bonding mode frequency curve from the continuum model.

2. Band structure of the infinite 1D chain

To obtain quantitative agreement of the discrete model with the continuum results, both τ and k_1 have to be changed with T. Physically, the need to modify k_1 reflects the fact that the bare resonator frequencies themselves depend on the prestress T in a nontrivial way that depends on geometry. Parameters $\kappa \approx 0.0575$ and $k_2 \approx 7.3724$ are fixed across all three prestress values, and parameters

k_1 and τ are determined by fitting the analytical dispersion relation to that from the continuum model at each value of the prestress T. The resulting fit parameters for the three prestress values in Fig. 3 are as follows: the flat band parameters are $k_1 \approx 0.5502$ and $\tau \approx 0.5217$; the acousticlike (top) band parameters are $k_1 \approx 1.4888$ and $\tau \approx 0.7677$; the optical-like (bottom) band parameters are $k_1 \approx 0.0381$ and $\tau \approx 0.3195$.

APPENDIX F: ANALYTICAL DERIVATION OF THE FLAT BAND IN THE DISCRETE MODEL

The existence of a perfectly flat band in the discrete model can be established provided that $\kappa' = 0$ in Eq. (G1). We start by assuming arbitrary κ and κ', and find the normal mode frequencies of the dynamical matrix $\mathbf{K}(q_x)$ from Eq. (G1) via $|\mathbf{K}(q_x) - \omega^2 \mathbf{I}| = 0$. This results in the quartic equation

$$(\omega^2)^2 - \omega^2(a + b\cos q_x + d + e\cos q_x)$$
$$+ (a + b\cos q_x)(d + e\cos q_x) - 2c^2(1 + \cos q_x) = 0. \tag{F1}$$

The coefficients of ω^2 and $\omega^0 = 1$ are minus the sum and the product of the two roots ω_1^2 and ω_2^2, respectively. If we require one of the roots to be a flat band, $\omega_1^2 = \alpha$ for some constant, then the other root must have the form

$$\omega_2^2 = \gamma + \delta\cos q_x + \phi\cos^2 q_x$$

to generate the requisite terms in the sum and product.

By matching coefficients of the $\cos q_x$ term and the remaining term in the sum and the product of the roots, we can find the relations between constants $\alpha, \gamma, \delta, \phi$ and a, b, c, d, e, and eventually the spring stiffnesses $k_1, k_2, \tau, \kappa, \kappa'$. We immediately find that one of b and e, i.e., one of the two bending stiffnesses, must be zero for the perfectly flat band to exist. Upon setting κ' to zero, the remaining parameters provide the band dispersion relations

$$\omega_1^2 = 2\tau + k_1,$$
$$\omega_2^2 = 2\tau + k_2 + 6\kappa + 2\kappa\cos q_x, \tag{F2}$$

with the constraint

$$\tau = -2\kappa + \sqrt{(k_2 - k_1)\kappa + (2\kappa)^2}. \tag{F3}$$

Note that this solution requires $k_2 > k_1$. However, as long as this condition is fulfilled, a tension τ can always be found to make the lower band completely flat.

The flat band is used to fit the band related to the fundamental mode from the continuum model at $T_{\mathrm{FB}} = 46.55$. For tension values other than T_{FB}, the band is dispersive and must be fitted using the solution to the quartic equation, Eq. (F1).
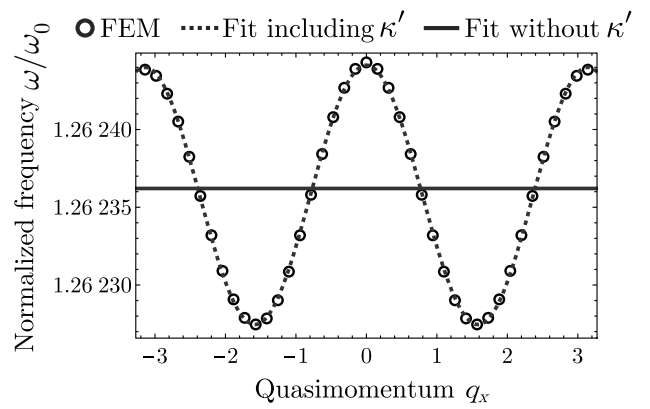

FIG. 8. Minute deviation from complete flatness. Fit functions are shown for the spring-mass model with bending stiffness κ only (solid line) at the junction point with the vertical spring stiffness k_2 and with additional bending stiffness κ' (dotted line) at the point with resonator stiffness k_1.

APPENDIX G: DEVIATION FROM A PERFECTLY FLAT BAND AND ADDITIONAL BENDING STIFFNESS

At the rescaled tension T_{FB}, the continuum model of the thin-plate resonator has a minute deviation from a perfectly flat band with bandwidth that is $10^{-3}\%$ of the mean band frequency (symbols in Fig. 8). For practical reasons and for demonstrating the tunable dispersion character of the fundamental band, such a small deviation is not consequential. However, even this variation can be incorporated in the discrete model by including an additional torsional spring, with rescaled stiffness κ', centered on the resonator degree of freedom (green mass springs in schematics). This addition modifies Eq. (3) from main text as

$$\mathbf{K}(q_x) = \begin{pmatrix} a + b\cos q_x & -c(1 + e^{-iq_x}) \\ -c(1 + e^{iq_x}) & d + e\cos q_x \end{pmatrix}, \tag{G1}$$

where $a = k_1 + 2\tau + 2\kappa + 4\kappa'$, $b = 2\kappa$, $c = \tau + 2\kappa + 2\kappa'$, $d = k_2 + 2\tau + 2\kappa' + 4\kappa$, and $e = 2\kappa'$.

Upon performing a fit with the additional parameter κ', the deviation from the perfectly flat band is quantitatively recovered (dotted line in Fig. 8).

APPENDIX H: DYNAMICAL SIMULATIONS

A *full-wave dynamical simulation* is performed via the finite-element method in COMSOL for the partial differential equation

$$\frac{\partial^2 u}{\partial t^2} + 2\gamma\frac{\partial u}{\partial t} + \nabla^4 u - T\nabla^2 u = 0. \tag{H1}$$

The second term in the above equation is added to the nondimensionalized equations of motion, Eqs. (2), to

incorporate the effect of dissipation in the continuum simulations. The damping ratio γ is chosen to reproduce the desired quality factor in the fundamental-mode dynamics of a single resonator. In our study, we use $\gamma \approx 8 \times 10^{-5}$, corresponding to a Q factor of approximately 6500. A predefined mesh in COMSOL called "Normal" calibrated for general physics is used for the full-wave dynamical simulation. The gradient operators and boundary conditions are implemented following the steps described in Appendix A. The element size parameters for this mesh are as follows: maximum element size of 6.7, minimum element size of 0.03, maximum element growth rate of 1.3, curvature factor of 0.3, and resolution of narrow regions equal to 1. A time-dependent solver called the generalized alpha is used with a time step of 0.01.

Classical dynamical simulation of the discrete 1D spring-mass model is implemented in C++ using the velocity Verlet algorithm. The position and velocity are evolved with time iteration i as

$$
\begin{aligned}
\mathbf{y}_{i+1} &+= \mathbf{v}_i \Delta t + \tfrac{1}{2}\mathbf{a}_i(\Delta t)^2, \\
\mathbf{v}_{i+1} &+= \tfrac{1}{2}(\mathbf{a}_{i+1} + \mathbf{a}_i)\Delta t,
\end{aligned}
\tag{H2}
$$

where $+=$ is the increment operator in the C language, and $\mathbf{y} = \{y_1, y_2, \ldots, y_n\}$, $\mathbf{v}$, and $\mathbf{a}$ are the particle displacements in the vertical direction, velocity, and acceleration, respectively. The acceleration a_n at lattice site n is

$$
\begin{aligned}
a_n = \frac{1}{m}[&(\tau + 2\kappa)(y_{n+1} + y_{n-1}) - \kappa(y_{n+2} + y_{n-2}) \\
&- (k_1 + 2\tau + 2\kappa)y_n - 2\zeta v_n] \quad \text{for even } n,
\end{aligned}
\tag{H3}
$$

and

$$
\begin{aligned}
a_n = \frac{1}{m}[&(\tau + 2\kappa)(y_{n+1} + y_{n-1}) \\
&- (k_2 + 4\tau + 8\kappa)y_n - 2\zeta v_n] \quad \text{for odd } n,
\end{aligned}
\tag{H4}
$$

based on the dynamical matrix in Eq. (3) of the main text. A time step $\Delta t = 0.01$ and a damping ratio $\zeta \approx 8 \times 10^{-5}$ are used for the simulation.

---

[1] Y.-F. Wang, Y.-Z. Wang, B. Wu, W. Chen, and Y.-S. Wang, Tunable and active phononic crystals and metamaterials, Appl. Mech. Rev. **72**, 040801 (2020).

[2] P. Wang, F. Casadei, S. Shan, J. C. Weaver, and K. Bertoldi, Harnessing Buckling to Design Tunable Locally Resonant Acoustic Metamaterials, Phys. Rev. Lett. **113**, 014301 (2014).

[3] K. Bertoldi, Harnessing instabilities to design tunable architected cellular materials, Annu. Rev. Mater. Res. **47**, 51 (2017).

[4] S. Babaee, N. Viard, P. Wang, N. X. Fang, and K. Bertoldi, Harnessing deformation to switch on and off the propagation of sound, Adv. Mater. **28**, 1631 (2016).

[5] S. Hedayatrasa, K. Abhary, M. S. Uddin, and J. K. Guest, Optimal design of tunable phononic bandgap plates under equibiaxial stretch, Smart Mater. Struct. **25**, 055025 (2016).

[6] R. K. Pal, J. Rimoli, and M. Ruzzene, Effect of large deformation pre-loads on the wave properties of hexagonal lattices, Smart Mater. Struct. **25**, 054010 (2016).

[7] F. Casadei, T. Delpero, A. Bergamini, P. Ermanni, and M. Ruzzene, Piezoelectric resonator arrays for tunable acoustic waveguides and metamaterials, J. Appl. Phys. **112**, 064902 (2012).

[8] J. Cha and C. Daraio, Electrical tuning of elastic wave propagation in nanomechanical lattices at MHz frequencies, Nat. Nanotechnol. **13**, 1016 (2018).

[9] K. Yi, M. Ouisse, E. Sadoulet-Reboul, and G. Matten, Active metamaterials with broadband controllable stiffness for tunable band gaps and non-reciprocal wave propagation, Smart Mater. Struct. **28**, 065025 (2019).

[10] N. Swinteck, P. Lucas, and P. A. Deymier, Optically tunable acoustic wave band-pass filter, AIP Adv. **4**, 124603 (2014).

[11] R. Feng and K. Liu, Tuning the band-gap of phononic crystals with an initial stress, Phys. B: Condens. Matter **407**, 2032 (2012).

[12] E. G. Barnwell, W. J. Parnell, and I. D. Abrahams, Tunable elastodynamic band gaps, Extreme Mech. Lett. **12**, 23 (2017).

[13] A. O. Krushynska, A. Amendola, F. Bosia, C. Daraio, N. M. Pugno, and F. Fraternali, Accordion-like metamaterials with tunable ultra-wide low-frequency band gaps, New J. Phys. **20**, 073051 (2018).

[14] R. K. Pal, M. Ruzzene, and J. J. Rimoli, Tunable wave propagation by varying prestrain in tensegrity-based periodic media, Extreme Mech. Lett. **22**, 149 (2018).

[15] Z.-N. Li, Y.-Z. Wang, and Y.-S. Wang, Tunable nonreciprocal transmission in nonlinear elastic wave metamaterial by initial stresses, Int. J. Solids Struct. **182-183**, 218 (2020).

[16] M. Fatemi and J. F. Greenleaf, Ultrasound-stimulated vibro-acoustic spectrography, Science **280**, 82 (1998).

[17] Y. Q. Fu, J. Luo, N.-T. Nguyen, A. Walton, A. J. Flewitt, X.-T. Zu, Y. Li, G. McHale, A. Matthews, and E. Iborra *et al.*, Advances in piezoelectric thin films for acoustic biosensors, acoustofluidics and lab-on-chip applications, Progress Mater. Sci. **89**, 31 (2017).

[18] A. A. Oliner, ed. *Acoustic Surface Waves*, Topics in Applied Physics (Springer, Berlin and Heidelberg, Germany, 1978), Vol. 24.

[19] F. Li, P. Anzel, J. Yang, P. G. Kevrekidis, and C. Daraio, Granular acoustic switches and logic elements, Nat. Commun. **5**, 5311 (2014).

[20] F. Zangeneh-Nejad and R. Fleury, Performing mathematical operations using high-index acoustic metamaterials, New J. Phys. **20**, 073001 (2018).

[21] Y. Wang, J.-p. Xia, H.-x. Sun, S.-q. Yuan, and X.-j. Liu, Binary-phase acoustic passive logic gates, Sci. Rep. **9**, 8355 (2019).

[22] N. Caselli, F. Intonti, F. Riboli, A. Vinattieri, D. Gerace, L. Balet, L. H. Li, M. Francardi, A. Gerardino, A. Fiore, and M. Gurioli, Antibonding ground state in photonic crystal molecules, Phys. Rev. B **86**, 035133 (2012).

[23] A. I. Yakimov, A. A. Bloshkin, and A. V. Dvurechenskii, Bonding–antibonding ground-state transition in coupled

Ge/Si quantum dots, Semicond. Sci. Technol. **24,** 095002 (2009).

[24] A. V. Zampetaki, J. Stockhofe, and P. Schmelcher, Degeneracy and inversion of band structure for wigner crystals on a closed helix, Phys. Rev. A **91,** 023409 (2015).

[25] S. Timoshenko and S. Woinowsky-Krieger, *Theory of Plates and Shells*, Engineering Mechanics Series (McGraw-Hill, New York, 1959).

[26] A. Blaikie, D. Miller, and B. J. Alemán, A fast and sensitive room-temperature graphene nanomechanical bolometer, Nat. Commun. **10,** 1 (2019).

[27] Z. Yosibash and R. Kirby, Dynamic response of various von-kármán non-linear plate models and their 3-d counterparts, Int. J. Solids Struct. **42,** 2517 (2005).

[28] G. Sweers, When is the first eigenfunction for the clamped plate equation of fixed sign?, Electron. J. Differential Equations (EJDE) [electronic only] **2001,** 285 (2001).

[29] B. M. Brown, E. B. Davies, P. K. Jimack, and M. D. Mihajlovi'c, On the accurate finite element solution of a class of fourth order eigenvalue problems, arXiv:math/9905038 [math.SP] (1999).

[30] P.-L. Yu, T. P. Purdy, and C. A. Regal, Control of Material Damping in High-Q Membrane Microresonators, Phys. Rev. Lett. **108,** 083603 (2012).

[31] K. H. Matlack, M. Serra-Garcia, A. Palermo, S. D. Huber, and C. Daraio, Designing perturbative metamaterials from discrete models, Nat. Materi. **17,** 323 (2018).

[32] G. Theocharis, O. Richoux, V. R. García, A. Merkel, and V. Tournat, Limits of slow sound propagation and transparency in lossy, locally resonant periodic structures, New J. Phys. **16,** 093017 (2014).

[33] A. M. v. d. Zande, R. A. Barton, J. S. Alden, C. S. Ruiz-Vargas, W. S. Whitney, P. H. Q. Pham, J. Park, J. M. Parpia, H. G. Craighead, and P. L. McEuen, Large-scale arrays of single-layer graphene resonators, , Nano Lett. **10,** 4869 (2010).

[34] M. Yuan, M. A. Cohen, and G. A. Steele, Silicon nitride membrane resonators at millikelvin temperatures with quality factors exceeding 108, Appl. Phys. Lett. **107,** 263501 (2015).

[35] T. Mei, J. Lee, Y. Xu, and P. X.-L. Feng, Frequency tuning of graphene nanoelectromechanical resonators via electrostatic gating, Micromachines **9,** 312 (2018).

[36] J. Güttinger, A. Noury, P. Weber, A. M. Eriksson, C. Lagoin, J. Moser, C. Eichler, A. Wallraff, A. Isacsson, and A. Bachtold, Energy-dependent path of dissipation in nanomechanical resonators, Nat. Nanotechnol. **12,** 631 (2017).

[37] M. Will, M. Hamer, M. Müller, A. Noury, P. Weber, A. Bachtold, R. V. Gorbachev, C. Stampfer, and J. Güttinger, High quality factor graphene-based two-dimensional heterostructure mechanical resonator, Nano Lett. **17,** 5950 (2017).

[38] D. Miller, A. Blaikie, and B. J. Alemán, Nonvolatile rewritable frequency tuning of a nanoelectromechanical resonator using photoinduced doping, Nano Lett. **20,** 2378 (2020).

[39] O. Derzhko, J. Richter, and M. Maksymenko, Strongly correlated flat-band systems: The route from heisenberg spins to hubbard electrons, Int. J. Modern Phys. B **29,** 1530007 (2015).

[40] D. Leykam and S. Flach, Perspective: Photonic flatbands, APL Photonics **3,** 070901 (2018).

[41] S. Wu and J. Mei, Flat band degeneracy and near-zero refractive index materials in acoustic crystals, AIP Adv. **6,** 015204 (2016).

[42] H. Zhu and F. Semperlotti, Double-Zero-Index Structural Phononic Waveguides, Phys. Rev. Appl. **8,** 064031 (2017).

[43] B. Li, Z. Li, J. Christensen, and K. T. Tan, Dual dirac cones in elastic lieb-like lattice metamaterials, Appl. Phys. Lett. **114,** 081906 (2019).

[44] T. Misumi and H. Aoki, New class of flat-band models on tetragonal and hexagonal lattices: Gapped versus crossing flat bands, Phys. Rev. B **96,** 155137 (2017).

[45] W. Maimaiti, A. Andreanov, H. C. Park, O. Gendelman, and S. Flach, Compact localized states and flat-band generators in one dimension, Phys. Rev. B **95,** 115135 (2017).

[46] J.-W. Rhim and B.-J. Yang, Classification of flat bands according to the band-crossing singularity of bloch wave functions, Phys. Rev. B **99,** 045107 (2019).

[47] R. Fleury, A. B. Khanikaev, and A. Alù, Floquet topological insulators for sound, Nat. Commun. **7,** 11744 (2016).

[48] H. Nassar, H. Chen, A. N. Norris, and G. L. Huang, Quantization of band tilting in modulated phononic crystals, Phys. Rev. B **97,** 014305 (2018).

[49] F. Zangeneh-Nejad and R. Fleury, Active times for acoustic metamaterials, Rev. Phys. **4,** 100031 (2019).

[50] C. Scheibner, W. T. M. Irvine, and V. Vitelli, Non-Hermitian Band Topology and Skin Modes in Active Elastic Media, Phys. Rev. Lett. **125,** 118001 (2020).

[51] C. Coulais, R. Fleury, and J. van Wezel, Topology and broken hermiticity, Nat. Phys. **17,** 9 (2021).

[52] J. D. Pillet, V. Benzoni, J. Griesmar, J. L. Smirr, and Ç. Ö. Girit, Nonlocal josephson effect in andreev molecules, Nano Lett. **19,** 7138 (2019).